

Where Not to Learn: Prior-Aligned Training with Subset-based Attribution Constraints for Reliable Decision-Making

Ruoyu Chen^{1,2} Shangquan Sun³ Xiaoqing Guo⁴ Sanyi Zhang⁵ Kangwei Liu^{1,2} Shiming Liu⁶
 Zhangcheng Wang⁷ Qunli Zhang⁶ Hua Zhang^{1,2} Xiaochun Cao⁸

Abstract

Reliable models should not only predict correctly, but also justify decisions with acceptable evidence. Yet conventional supervised learning typically provides only class-level labels, allowing models to achieve high accuracy through shortcut correlations rather than the intended evidence. Human priors can help constrain such behavior, but aligning models to these priors remains challenging because learned representations often diverge from human perception. To address this challenge, we propose an attribution-based human prior alignment method. We encode human priors as input regions that the model is expected to rely on (e.g., bounding boxes), and leverage a highly faithful subset-selection-based attribution approach to expose the model’s decision evidence during training. When the attribution region deviates substantially from the prior regions, we penalize reliance on off-prior evidence, encouraging the model to shift its attribution toward the intended regions. This is achieved through a training objective that imposes attribution constraints induced by the human prior. We validate our method on both image classification and click decision tasks in MLLM-based GUI agent models. Across conventional classification and autoregressive generation settings, human prior alignment consistently improves task accuracy while also enhancing the model’s decision reasonability.

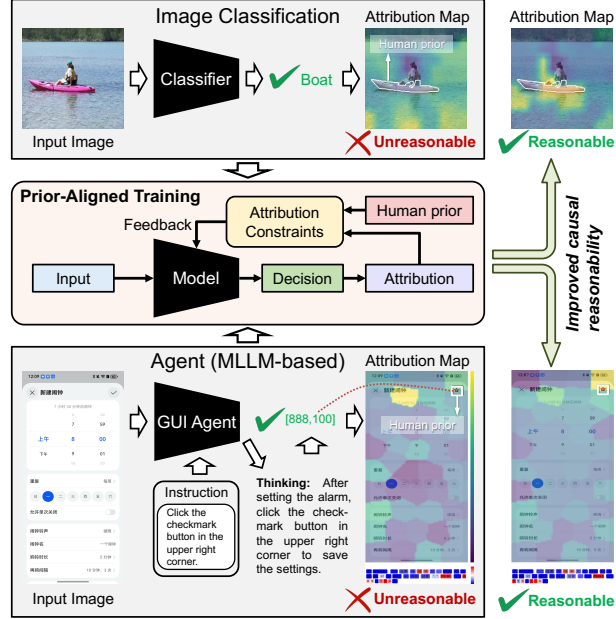


Figure 1. Correct outputs do not guarantee reasonable decision evidence: both a classifier and an MLLM-based GUI agent can succeed while their attribution maps violate human priors. We propose attribution-guided, prior-constrained alignment training to push evidence toward human-prior regions and improve causal reasonability.

1. Introduction

Machine learning has recently achieved remarkable progress, with large-scale vision and multimodal models delivering strong performance across a wide range of tasks (Li et al., 2025b;a). As these models are increasingly deployed in real-world applications, reliability becomes a central concern (Kuznetsov et al., 2024). Reliable models should not only predict correctly, but also rely on acceptable and task-relevant evidence. However, during training, models may learn shortcut correlations (Geirhos et al., 2020; Kauffmann et al., 2025), leading to seemingly correct outputs that are supported by inappropriate evidence and can fail unpredictably in safety-critical or interactive settings, as shown in Fig. 1.

¹Institute of Information Engineering, Chinese Academy of Sciences ²University of Chinese Academy of Sciences ³College of Computing and Data Science, Nanyang Technological University ⁴Department of Computer Science, Hong Kong Baptist University ⁵Communication University of China ⁶Huawei ⁷University of Science and Technology of China ⁸School of Cyber Science and Technology, Shenzhen Campus of Sun Yat-sen University. Correspondence to: Ruoyu Chen <cry-explorer@gmail.com>, Hua Zhang <zhanghua@iie.ac.cn>, Xiaochun Cao <caoxiaochun@mail.sysu.edu.cn>.

Standard supervised learning typically provides only class-level supervision, specifying what the correct output should be while leaving the decision evidence largely unconstrained (D’Amour et al., 2022; Geirhos et al., 2018; Rosenfeld et al., 2021). As a result, even large-scale models can be driven to rely on the easiest or most statistically salient correlations rather than the intended causal or semantically meaningful features (D’Amour et al., 2022; Turpin et al., 2023). Human priors can mitigate this issue by constraining what a reasonable decision should rely on. Here, human priors refer to human-recognizable cues about which input components (e.g., objects/regions/attributes) should be relied on for the prediction, typically provided as weak supervision such as sparse clicks, bounding boxes, or saliency annotations. However, aligning models to such priors remains difficult, because model representations and internal decision processes often diverge from human perception (Feather et al., 2019; Poursabzi-Sangdeh et al., 2021; Ngo et al., 2024).

Attribution methods (Chen et al., 2024; 2025a) aim to expose the input evidence that a trained model actually relies on for its predictions. When attribution is sufficiently faithful, meaning that it truthfully reflects the causal evidence underlying the model’s decision. However, most existing attribution methods are primarily descriptive: they can explain model behavior, but cannot be directly used to target the model’s deficiencies. Some works leverage attribution signals for targeted model correction. RRR (Ross et al., 2017) and XIL (Schramowski et al., 2020) improve decision rationality and accuracy by suppressing gradients outside human-prior regions at the input/feature level, while MEGL (Zhang et al., 2024) encourages feature activation maps to align with human annotations to learn more plausible evidence. However, these methods (i) rely on low-faithfulness attributions that may fail to capture the true decision evidence, and (ii) enforce hard, uniform suppression/enhancement (e.g., pushing all non-prior regions toward zero), ignoring that different regions may contribute unequally.

To address these challenges, we propose an attribution-based human prior alignment framework that can be instantiated for both image classification and autoregressive generation in (M)LLMs, as shown in Fig. 1. We represent human priors as expected input regions, such as object bounding boxes or interface elements, and use the state-of-the-art subset-selection-based attribution method (Chen et al., 2024; 2025a) during training to identify the minimal decision-sufficient regions. We do not enforce a direct, global alignment to human priors. Instead, we penalize reliance on non-prior regions only when the model’s most salient attributed evidence deviates from the prior. When the top-attributed evidence is consistent with human expectations, we refrain from intervening and allow other regions to contribute freely. This yields a training objective that guides decision evidence toward the intended regions with-

out sacrificing predictive performance.

We evaluate the proposed framework across both image classification tasks and click decision tasks in multimodal large language model-based GUI (Graphical User Interface) agent (Zhang et al., 2025c) settings. These experiments encompass both conventional discriminative prediction and autoregressive decision-making scenarios. Empirically, human prior alignment consistently improves task accuracy while simultaneously enhancing decision reasonability, indicating that constraining decision evidence can yield models that are not only more interpretable but also more robust and effective.

In summary, the contributions of this paper are:

- We propose an attribution alignment framework that leverages human priors to enforce causal reasonability, simultaneously boosting model performance and interpretability.
- We design an alignment objective built on faithful subset-selection attribution that penalizes only unreasonable off-prior decision evidence, thereby suppressing spurious reliance outside the human prior.
- Experiments on both image classification and GUI agent click decision tasks demonstrate the general applicability of our method across discriminative and decision-making settings, improving both predictive performance and attribution reasonability.

2. Related Work

Attribution technologies aim to explain the decision evidence of a model prediction by assigning relevance to input components such as pixels, regions, or tokens. Existing approaches differ in mechanism, including gradient-based methods (Selvaraju et al., 2020; Zhao et al., 2024; Zhang et al., 2025a; Xing et al., 2025), perturbation-based methods (Petsiuk et al., 2018; Novello et al., 2022), Shapley value-based methods (Lundberg & Lee, 2017; Sun et al., 2023), and attention-based methods (Li et al., 2025c). Despite their empirical success, these methods face a core challenge of faithfulness, namely whether the attributed evidence reflects the causal factors driving the decision, which has motivated minimal sufficiency formulations that seek the smallest evidence subset preserving the original prediction. Recent subset selection-based methods (Chen et al., 2024; 2025c;b;a) achieve higher faithfulness than other attribution methods, so we use them to guide model training toward more reasonable decision evidence.

Attribution-guided learning studies how attribution signals can be incorporated into training to shape model behavior beyond output supervision (Gao et al., 2024). Some

works encourage sparsity or smoothness by regularizing gradient-based attributions during training, but often at the cost of accuracy (Erion et al., 2021; Han et al., 2021; Pillai et al., 2022). Other works use counterfactual attribution for data augmentation to improve generalization (Chen et al., 2025d;e), but do not directly improve attribution reasonableness. Attribution-based human prior alignment methods can improve the reasonableness of model decisions (Ross et al., 2017; Schramowski et al., 2020; Selvaraju et al., 2019; Zhang et al., 2023). However, they often rely on low-faithfulness attributions (e.g., Grad-CAM (Selvaraju et al., 2020) or LIME (Ribeiro et al., 2016)) to guide training, which may limit reasonability gains when the attributions fail to reflect true decision evidence. In this paper, we constrain training with highly faithful attribution methods (LIMA (Chen et al., 2024; 2025c) and EAGLE (Chen et al., 2025a)) and human priors, improving both attribution reasonability and model performance.

3. Preliminaries and Problem Statement

3.1. Subset-selection based Attribution

Attribution methods seek to explain model decisions by quantifying the dependence of a prediction on individual input components. Subset-selection based attribution ranks sub-regions in the entire inputs by iteratively selecting compact decision-supporting subsets. Regions selected earlier are deemed more influential, defined as follows.

Definition 3.1 (Subset-Selection-Based Attribution). Given an input \mathbf{x} , a trained model f , and an objective set function $\mathcal{F}(\cdot)$, subset-selection-based attribution sparsifies \mathbf{x} into sub-regions $\mathcal{V} = \{v_1, \dots, v_n\}$ and produces a ranking over \mathcal{V} by solving

$$\pi = \max_{\pi \in \mathcal{P}(\mathcal{V})} \sum_{r=1}^{|\mathcal{V}|} \mathcal{F}(\pi_{:r}), \quad (1)$$

where π is an ordering of \mathcal{V} , $\pi_{:r}$ denotes the prefix set consisting of the first r elements in π , and $\mathcal{P}(\mathcal{V})$ is the set of all permutations of \mathcal{V} . This objective can be efficiently optimized via greedy search or its accelerated variants.

From this perspective, attribution is cast as a subset selection problem over \mathcal{V} , where decision evidence is characterized by compact, decision-supporting subsets and their induced ordering.

3.2. Problem Statement

Attribution-based constrained training is formulated by introducing an attribution regularization term $\mathcal{L}_{\text{human}}$ that encourages consistency between model attributions and human

priors. The resulting optimization objective is

$$\min_{\theta} \mathbb{E}_{(x, y, H) \sim \mathcal{D}} \left[\underbrace{\mathcal{L}_{\text{task}}(f_{\theta}(x), y)}_{\text{task supervision}} + \lambda \underbrace{\mathcal{L}_{\text{human}}(\mathcal{A}(f_{\theta}(x), y), H)}_{\text{human prior alignment}} \right], \quad (2)$$

where H denotes a human prior associated with sample x , and \mathcal{A} is the attribution method. Importantly, H serves as weak guidance rather than exact causal ground truth, and is used to constrain the model’s attributed decision evidence toward human-recognized regions. Such constraints aim to improve the causal rationality of model decisions, thereby enhancing model performance, robustness, and interpretability.

4. Method

This section introduces our attribution-based prior-constrained alignment algorithm. Section 4.1 presents the alignment principle. Section 4.2 then details the loss-function instantiation. Finally, Section 4.3 describes the overall training objective and optimization procedure.

4.1. Evidence-Level Alignment Principle

We align model behavior with human priors by constraining decision evidence rather than internal representations. This relies on subset-selection-based attribution, which identifies compact decision-supporting subsets and their induced ordering, and is more faithful than gradient- or attention-based methods in reflecting the evidence driving model decisions. Let \mathcal{V} denote the set of input sub-regions and H denote a human prior specified over the input space, such as bounding boxes or masks. For a given prediction, attribution ranks regions in \mathcal{V} by their influence on the decision. When the most influential evidence sufficiently overlaps with H , no constraint is imposed. When highly ranked evidence lies largely outside H , the model may rely on unintended cues, which should be discouraged during training.

Alignment is imposed asymmetrically: only off-prior decision evidence is penalized, while evidence consistent with the prior remains unconstrained. This avoids over-regularization and preserves flexibility within human-recognized regions. The same principle applies to both discriminative classification and autoregressive decision-making in MLLM-based GUI agents. In practice, we instantiate a black-box subset-selection-based attribution framework using LIMA (Chen et al., 2024; 2025c) for image classification models and EAGLE (Chen et al., 2025a) for MLLM-based GUI agents. As attribution relies only on model inputs and outputs, the framework generalizes across diverse model architectures.

4.2. Alignment with Subset-based Attribution

We instantiate the prior constrained training using the subset-based attribution framework in Section 3.1, which produces an ordering over sub-regions \mathcal{V} by decision influence. Let $\pi = (v_{\pi_1}, v_{\pi_2}, \dots, v_{\pi_{|\mathcal{V}|}})$ denote the ranking over sub-regions \mathcal{V} induced by attribution, where regions appearing earlier are more influential. Let H denote the human prior specified over the input space (e.g., bounding boxes or masks). Since H may not lie in the same discrete space as \mathcal{V} , we define an overlap function $\phi(v, H) \in [0, 1]$, which measures the spatial consistency between a region v and the human prior H (e.g., IoU or mask coverage). A region is considered off-prior when $\phi(v, H)$ is small.

Deviation loss: To prevent the most influential attribution region from deviating from the human prior during training, we introduce a *Deviation Loss*. Since subset-selection-based attribution ranks regions according to a set function $\mathcal{F}(\cdot)$, deviations from the prior are addressed by suppressing the contribution of the top-ranked region. Specifically, when the most influential region v_{π_1} exhibits low consistency with the human prior, we reduce its utility score $\mathcal{F}(v_{\pi_1})$ to discourage reliance on this region. The resulting optimization objective is

$$\mathcal{L}_{\text{deviation}} = \sum_{i=1}^b \mathcal{F}(v_{(i, \pi_1)}) \cdot \mathbf{1} [\phi(v_{(i, \pi_1)}, H_i) < \tau], \quad (3)$$

where b denotes the batch size, $v_{(i, \pi_1)}$ is the most influential attribution region for the i -th sample, τ is a threshold determining consistency with the human prior, and $\mathbf{1}[\cdot]$ is the indicator function. Intuitively, no penalty is applied when the most influential attribution region lies within the human prior. When the primary attribution region falls outside the prior, its explanatory influence should be limited, and the corresponding utility score \mathcal{F} is therefore suppressed.

Redundancy loss: Beyond constraining the primary attribution region, we further regulate *higher-order attribution regions*, referring to all attribution results beyond the top-ranked one. When such higher-order regions fall outside the human prior, their contribution to the model’s decision should be limited, as accumulating evidence from unintended regions leads to redundant and potentially spurious decision support. Intuitively, off-prior regions should not provide substantial additional gains once the primary evidence has been identified. Since subset-based attribution constructs decision evidence sequentially via marginal gains of the set function $\mathcal{F}(\cdot)$, we suppress excessive marginal contributions from higher-order off-prior regions. This redundancy loss mitigates the accumulation effect in multi-region combinations, preventing off-prior regions from jointly contributing to the prediction and introducing shortcut cues.

Algorithm 1 Prior constrained training with subset-based attribution

Input: training data (\mathbf{x}_i, y_i, H_i) , alignment interval T , loss weights λ_1, λ_2 , attribution length k
Output: trained model parameters θ
 Initialize model parameters θ
for $t = 1$ **to** T_{max} **do**
 Sample a mini-batch $\{(\mathbf{x}_i, y_i, H_i)\}_{i=1}^b$
 Compute task loss $\mathcal{L}_{\text{task}}$
 if $t \bmod T = 0$ **then**
 Initialize $\mathcal{L}_{\text{deviation}} = 0, \mathcal{L}_{\text{redundancy}} = 0$
 for each sample i in the batch **do**
 if prediction of sample i is correct **then**
 Compute top- k attribution ranking π using LIMA or EAGLE
 Compute deviation loss from top-ranked region v_{π_1}
 Compute redundancy loss from higher-order regions
 end if
 end for
 $\mathcal{L}_{\text{total}} \leftarrow \mathcal{L}_{\text{task}} + \lambda_1 \mathcal{L}_{\text{deviation}} + \lambda_2 \mathcal{L}_{\text{redundancy}}$
 else
 $\mathcal{L}_{\text{total}} \leftarrow \mathcal{L}_{\text{task}}$
 end if
 Update model parameters θ using $\nabla \mathcal{L}_{\text{total}}$
end for

The objective is

$$\mathcal{L}_{\text{redundancy}} = \sum_{i=1}^b \sum_{r=2}^k \text{ReLU}(\Delta_{i,r} - \gamma) \cdot \mathbf{1} [\phi(v_{(i, \pi_r)}, H_i) < \tau], \quad (4)$$

where $\Delta_{i,r} = \mathcal{F}(\pi_{:,r}) - \mathcal{F}(\pi_{:,r-1})$ denotes the marginal gain contributed by the region at rank r , given the previously selected prefix regions, γ controls the acceptable marginal gain for off-prior regions, and k denotes the maximum number of sub-regions considered during attribution.

4.3. Overall Training Objective

We optimize the model using a mixed training objective that alternates between standard task supervision and evidence-level alignment. Specifically, alignment losses are applied only at regular intervals to reduce computational overhead and to avoid over-constraining the model during training.

Formally, let t denote the training step and T the alignment interval. When $t \bmod T = 0$, alignment is applied only to training samples that are correctly predicted by the model. For such samples, the optimization objective is

$$\mathcal{L} = \mathcal{L}_{\text{task}} + \lambda_1 \mathcal{L}_{\text{deviation}} + \lambda_2 \mathcal{L}_{\text{redundancy}}, \quad (5)$$

where $\mathcal{L}_{\text{task}}$ denotes the standard task loss. For samples

Table 1. Evaluation of attribution-based prior alignment methods for image classification models on the Saliency-Bench and ImageNet-S datasets. Both model performance (accuracy) and decision rationality are reported, with rationality measured by the Point Game and accuracy conditioned on successful Point Game outcomes.

Datasets	Human Prior	Models	Methods	Attributions	Top-1 Acc.	Top-2 Acc.	Point Game	Top-1 Acc. (PG=1)	Training Time / Epoch
Saliency-Bench (Zhang et al., 2025b)	Masks	CLIP (Radford et al., 2021)	Fine-tuning	-	0.6076	0.7847	0.5231	0.9044	43s
			RRR (Ross et al., 2017)	Input Gradient	0.6030	0.7821	0.5253	0.8943	1m 47s
			XIL (Schramowski et al., 2020)	Grad-ECLIP	0.6400	0.7891	0.5327	0.9045	1m 21s
			MEGL (Zhang et al., 2024)	Grad-ECLIP	0.6354	8180	0.5318	0.9004	1m 48s
			Ours	LIMA	0.6551	0.8264	0.5648	0.9192	7m 50s
		ViT (base) (Dosovitskiy et al., 2021)	Fine-tuning	-	0.5150	0.7350	0.4363	0.7786	37s
			RRR (Ross et al., 2017)	Input Gradient	0.5370	0.7512	0.4509	0.6530	1m 23s
			XIL (Schramowski et al., 2020)	Grad-ECLIP	0.5139	0.6968	0.4397	0.8087	1m 07s
			MEGL (Zhang et al., 2024)	Grad-ECLIP	0.5359	0.7338	0.5145	0.8242	1m 11s
			Ours	LIMA	0.5694	0.7639	0.5463	0.8519	2m 42s
	ResNet-101 (He et al., 2016)	CLIP (Radford et al., 2021)	Fine-tuning	-	0.5498	0.7569	0.6235	0.7694	35s
			RRR (Ross et al., 2017)	Input Gradient	0.5498	0.7604	0.6076	0.7857	56s
			XIL (Schramowski et al., 2020)	Grad-CAM	0.5521	0.7616	0.6725	0.8679	41s
			MEGL (Zhang et al., 2024)	Grad-CAM	0.5451	0.7662	0.6315	0.8344	47s
			Ours	LIMA	0.5590	0.7662	0.6984	0.8782	1m 04s
ImageNet-S (Gao et al., 2022)	Masks	CLIP (Radford et al., 2021)	Fine-tuning	-	0.7969	0.8888	0.7001	0.7093	2m 18s
			RRR (Ross et al., 2017)	Input Gradient	0.7898	0.8861	0.7051	0.7642	5m 43s
			XIL (Schramowski et al., 2020)	Grad-ECLIP	0.7807	0.8786	0.7535	0.8042	2m 42s
			MEGL (Zhang et al., 2024)	Grad-ECLIP	0.7857	0.8795	0.7556	0.7942	3m 05s
			Ours	LIMA	0.7974	0.8895	0.7712	0.8377	8m 34s
		ViT (base) (Dosovitskiy et al., 2021)	Fine-tuning	-	0.6713	0.7728	0.8041	0.8762	1m 04s
			RRR (Ross et al., 2017)	Input Gradient	0.6868	0.7912	0.7923	0.8580	1m 30s
			XIL (Schramowski et al., 2020)	Grad-ECLIP	0.6952	0.7971	0.8035	0.8514	1m 14s
			MEGL (Zhang et al., 2024)	Grad-ECLIP	0.6969	0.8024	0.8143	0.8654	1m 18s
			Ours	LIMA	0.7208	0.8087	0.8226	0.8878	2m 54s
	ResNet-101 (He et al., 2016)	CLIP (Radford et al., 2021)	Fine-tuning	-	0.7071	0.8011	0.8453	0.8814	23s
			RRR (Ross et al., 2017)	Input Gradient	0.7073	0.8076	0.8364	0.8532	1m 10s
			XIL (Schramowski et al., 2020)	Grad-CAM	0.7225	0.8182	0.8491	0.8904	1m 14s
			MEGL (Zhang et al., 2024)	Grad-CAM	0.7212	0.8158	0.8303	0.8522	1m 29s
			Ours	LIMA	0.7245	0.8186	0.8672	0.9040	2m 39s

that are incorrectly predicted, as well as for all steps where $t \bmod T \neq 0$, the model is optimized using only the task loss. This intermittent and conditional alignment strategy ensures that attribution-based constraints are imposed only when the model’s predictions are reliable, allowing efficient learning of task-relevant representations while periodically correcting reliance on off-prior decision evidence, leading to stable training and improved generalization. The overall training procedure is summarized in Algorithm 1.

5. Experiments

5.1. Experimental Setup

Datasets. We evaluate the proposed method on two representative tasks: image classification and a MLLM-based GUI agent clicking task. For image classification, we use two datasets with high-quality object-level annotations. ImageNet-S (Gao et al., 2022) is a curated subset of ImageNet with 919 categories and pixel-level segmentation masks, while Saliency-Bench (Zhang et al., 2025b) is constructed from MS COCO with high-quality object annotations. These datasets enable a challenging evaluation of both predictive performance and attribution faithfulness. For the GUI agent task, UI elements (e.g., buttons and icons) encode human priors over actionable targets. We collect 936 single-step Android clicking tasks with annotations of click locations and UI element bounding boxes, enabling a controlled evaluation of decision rationality in domain-specific MLLMs. The dataset will be released.

Baselines. We compare with representative attribution-based prior alignment baselines, including RRR (Ross et al., 2017), which penalizes input-level gradients (Simonyan et al., 2014) on non-prior regions, XIL (Selvaraju et al., 2019), which suppresses Grad-CAM (Selvaraju et al., 2020) activations outside prior regions at the feature level, and MEGL (Zhang et al., 2024), which aligns Grad-CAM maps with mask annotations using an ℓ_1 loss. For ViT-based architectures, Grad-CAM is replaced with Grad-ECLIP (Zhao et al., 2024).

Implementation Details. For classification models, we compute attributions and perform prior alignment once every 10 training steps. For GUI-agent models, attributions are computed once every 5 steps. The loss balancing coefficients, λ_1 and λ_2 , are both set to 0.5. During training, the subset-selection-based attribution sparsifies each image into 50 sub-regions. The attribution search selects at most 10 sub-regions and early-stops once the prediction confidence of the selected subset exceeds 0.8. We apply the attribution-alignment losses only to samples that are correctly predicted with confidence above 0.75, otherwise, the model is trained with the standard task loss only. More details please see the Appendix.

5.2. Evaluation on Image Classification

We first validate our method on image classification tasks, where the selected datasets provide both class labels and object masks as human priors. In addition to comparing against direct fine-tuning to assess the benefit of prior su-

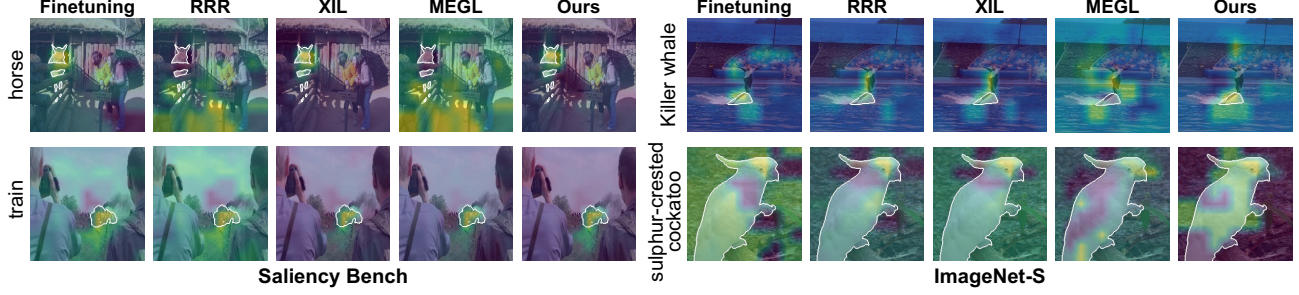


Figure 2. Qualitative comparison on Saliency-Bench and ImageNet-S. For each method, we visualize LIMA-based attributions on the same inputs; white masks indicate human priors (target object regions).

Table 2. Ablation studies on the deviation loss and the redundancy loss on the Saliency Bench dataset.

Models	Deviation loss	Redundancy loss	Accuracy	Point Game
CLIP	✗	✗	0.6076	0.5231
	✓	✗	0.6525	0.5575
	✓	✓	0.6551	0.5648
ViT	✗	✗	0.5150	0.4363
	✓	✗	0.5359	0.5238
	✓	✓	0.5690	0.5463
ResNet	✗	✗	0.5498	0.6235
	✓	✗	0.5535	0.6849
	✓	✓	0.5590	0.6984

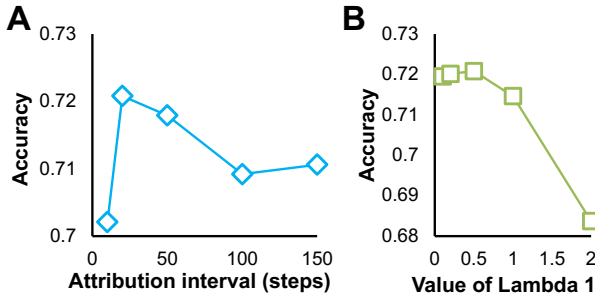


Figure 3. Impact of training hyperparameters on model performance. **A.** Effect of the attribution interval on validation accuracy. **B.** Effect of the loss balancing coefficient λ_1 on validation accuracy.

pervision, we include attribution-based baselines that adopt different attribution methods and alignment strategies. We report top-1 accuracy and decision rationality measured by Point Game (Zhang et al., 2018), which evaluates whether predictions attend to target objects rather than background regions. Since LIMA (Chen et al., 2024; 2025c) provides the highest attribution faithfulness among existing methods, we adopt LIMA-based attributions for evaluation to ensure a consistent and reliable assessment of decision rationality, regardless of the attribution strategies used during training.

As shown in Table 1, across backbones (CLIP (Radford et al., 2021), ViT (Dosovitskiy et al., 2021), and ResNet (He et al., 2016)) on Saliency-Bench, our method consistently

Table 3. Validation accuracy with Gaussian noise on the Saliency Bench dataset.

Models	Methods	Clean Val. Accuracy	Noisy Val. Accuracy
CLIP	Fine-tuning	0.6076	0.5995
	Ours	0.6551	0.6157
ResNet	Fine-tuning	0.5498	0.4167
	Ours	0.5590	0.4572

improves Point Game (e.g., from 0.4363 to 0.5463 on ViT) while also increasing top-1 accuracy (e.g., from 0.5150 to 0.5694 on ViT and from 0.6076 to 0.6551 on CLIP). On ImageNet-S, the gains in top-1 accuracy are relatively modest but remain positive (e.g., improve 4.95 points on ViT and 1.74 points on ResNet-101), which we attribute in part to the limited number of training images per category in this subset, while rationality improves where available. We further report top-1 accuracy conditioned on successful Point Game outcomes. Notably, our method yields substantial gains on this metric (e.g., from 0.7093 to 0.8377 on CLIP for ImageNet-S), suggesting that when the model attends to the target object as expected, its predictions become markedly more reliable. Compared with prior-alignment baselines that rely on input gradients or Grad-CAM variants, the improvements are more consistent on rationality-related metrics, indicating a higher effective upper bound when enforcing priors with more faithful attributions.

Figure 2 shows qualitative results. We visualize LIMA attributions for all models, regardless of the attribution strategy used during training. Notably, image classification inputs may contain multiple co-occurring objects, where spurious or non-target objects can distract the decision evidence. Compared with prior-alignment baselines, our method yields attributions that are more concentrated on the human-prior target regions, indicating that the resulting predictions rely less on irrelevant objects or background cues.

Table 4. Evaluation on the GUI agent clicking task with AgentCPM-GUI. Standard SFT (LoRA) is compared with attribution-based alignment (LoRA). Task performance is reported by click success rate and distance error, and reliability is measured by Point Game and metrics conditioned on successful Point Game outcomes (click success rate and distance error when PG=1).

Methods	Task Performance		Point Game (↑)	Reliability Metrics	
	Click success rate (↑)	Distance error (↓)		Click success rate (PG=1) (↑)	Distance error (PG=1)
SFT (LoRA)	84.61%	94.71	0.8153	96.22%	7.11
Ours (LoRA)	89.23%	78.64	0.8615	100%	0.0

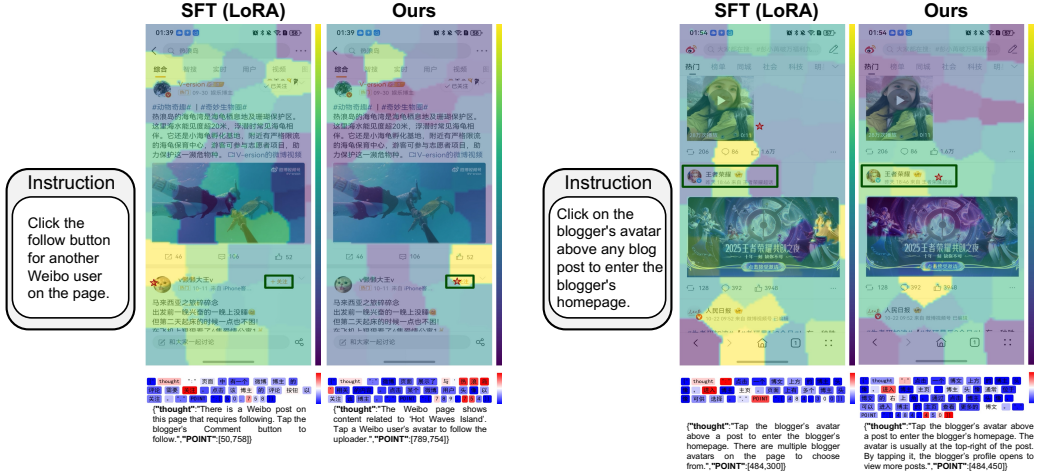


Figure 4. Qualitative GUI agent results comparing SFT with LoRA adaptation and the proposed our method, together with attribution heatmaps, predicted click locations (stars), and human-prior target bounding boxes.

5.3. Ablation Study

Ablation of the components. Table 2 presents ablations of the deviation loss and redundancy loss across different backbones on Saliency-Bench dataset. Overall, the deviation loss brings consistent gains in both accuracy and decision reasonability. This indicates that explicitly penalizing reliance on off-prior evidence can effectively steer the model to ground its most influential evidence on human-recognized regions, which improves not only prediction performance but also prior-consistent explanations. In contrast, the redundancy loss mainly affects the quality of the explanation: when combined with the deviation loss, it yields an additional (typically mild) improvement in Point Game, while its impact on accuracy is limited. This behavior aligns with its design goal, by accounting for the cumulative effect of selected regions, the redundancy term suppresses repeated/overlapping evidence and encourages more efficient evidence allocation, thereby slightly enhancing decision reasonability.

Parameter sensitivity analysis. We conduct a parameter sensitivity study on ImageNet-S using the ViT backbone, focusing on (i) the step interval for applying attribution-based prior constraints during training and (ii) the weighting coefficient of the deviation loss. Figure 3A shows that applying the constraint more frequently (i.e., using a smaller interval) can improve classification accuracy, but enforcing

it too often may disrupt optimization of the primary task and degrade performance. Figure 3B indicates that accuracy remains stable for small-to-moderate λ_1 , while overly large λ_1 causes a clear drop, suggesting that the deviation loss should be weighted moderately to avoid overwhelming the main objective.

Robustness for noise. Table 3 compares robustness under Gaussian noise corruption at evaluation time on the Saliency Bench dataset. Specifically, we add random Gaussian noise to validation images and report the resulting accuracy. Our method consistently outperforms standard fine-tuning on the noisy validation set, indicating stronger noise robustness. This suggests that prior-aligned evidence constraints help the model rely on stable, semantically meaningful regions rather than brittle spurious cues, thereby improving robustness to input perturbations.

5.4. Mitigation to MLLM-based GUI Agent

Next, we validate our method in a GUI agent setting. We use AgentCPM-GUI (Zhang et al., 2025c), a reasoning-oriented MLLM that produces both thinking and a final decision (click action). We adopt supervised fine-tuning (SFT) as the primary training paradigm, using data that contains the target decision together with GPT-distilled thinking traces. Our goal is to improve the consistency

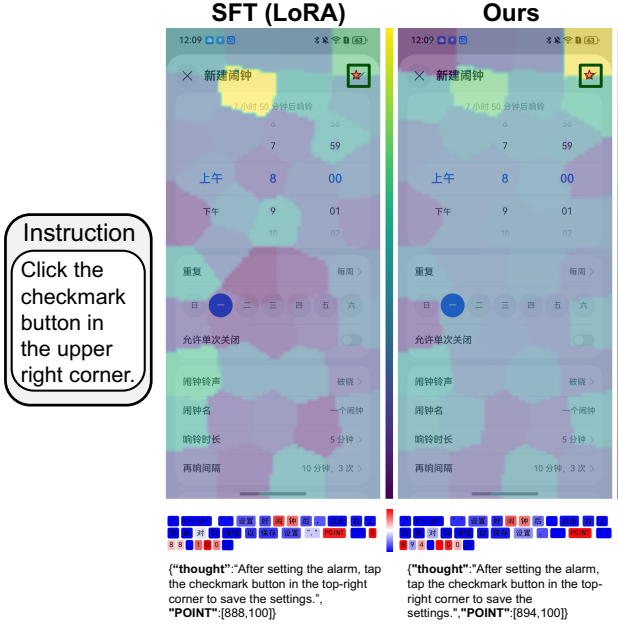


Figure 5. GUI clicking example comparing SFT with LoRA adaptation and our method, showing attribution maps and correct clicks on the target checkmark.

between the decision evidence expressed in `thinking` and the executed `decision` via attribution-based consistency regularization. We employ EAGLE (Chen et al., 2025a) for attribution, which is tailored to MLLMs. Since there are no established attribution-alignment baselines for MLLMs in this GUI clicking setup, we mainly evaluate the gains of our method over standard SFT. Note that SFT already injects prior information to some extent, as the training supervision explicitly specifies the click target. The evaluation metrics are described in Appendix A.4.

Table 4 summarizes the results on the GUI agent clicking task. The findings are analyzed from three aspects: functional performance, content understanding with attribution consistency, and decision reliability. With supervised fine-tuning (SFT) and LoRA adaptation, AgentCPM-GUI achieves a click success rate of 84.61% and a distance error of 94.71. After introducing attribution constraints, the click success rate increases to 89.23% (an absolute gain of 4.62%), while the distance error decreases to 78.64 (a relative reduction of 16.96%). These results indicate that our attribution-prior alignment improves task performance and yields more stable clicks by encouraging attention to task-relevant regions, Figure 4 shows some examples.

Next, decision rationality is examined for the reasoning agent. EAGLE is used to attribute the generation process without additional annotations. As shown in Table 4, the Point Game (PG) score increases from 0.8153 with SFT to 0.8615 with our method (a relative gain of 5.67%), indicating stronger consistency between reasoning–decision

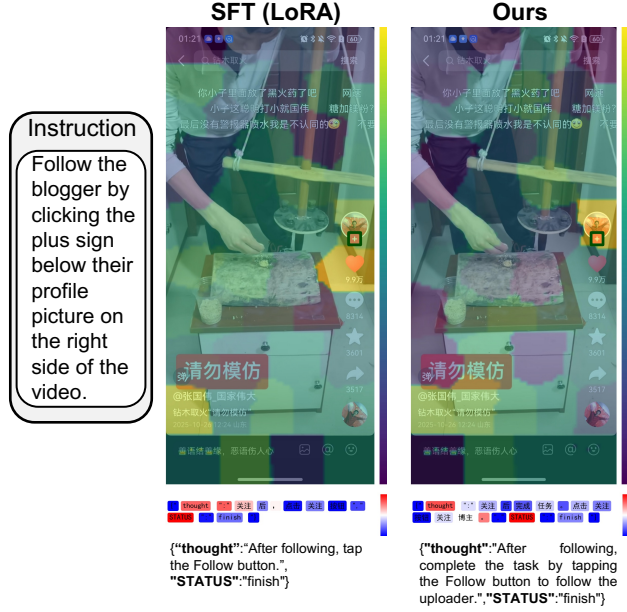


Figure 6. Failure-case comparison on the GUI agent task.

evidence and human-prior target regions. Figure 5 further provides a qualitative comparison: although both methods produce correct clicks, SFT does not always attend to the target region during `thinking`, whereas our method yields more evidence-consistent thinking and decision.

Reliability is further analyzed on samples where attributions match human priors (PG= 1): as shown in Table 4, the click success rate increases from 96.22% to 100%, and the distance error drops from 7.11 to 0. While the 100% rate may be influenced by the limited evaluation set, the consistent trend indicates that prior-consistent evidence correlates with more robust behavior, and our method increases the coverage of such high-reliability decisions by improving thinking and decision evidence consistency.

Failure analysis. Next, failure cases are analyzed in Figure 6. In these examples, neither model outputs a `POINT`; instead, both return a `STATUS`. The attribution results indicate that the `thought` from both SFT and our method captures the instruction intent, but the supporting evidence differs: SFT focuses on the `like` button region, whereas our method concentrates on the `follow` button. This suggests that our method produces more semantically grounded `thought` evidence, even when the final action format is incorrect.

6. Conclusion

In this paper, we argued that reliable models should not only produce correct outputs, but also rely on acceptable, task-relevant evidence. We proposed a prior-aligned train-

ing framework that enforces evidence-level constraints using faithful subset-selection attribution. Human priors are encoded as expected input regions (e.g., object masks or UI-element bounding boxes), and the model’s decision evidence is explicitly exposed during training via subset-based attributions. Experiments on both image classification and GUI clicking tasks show that prior-constrained attribution alignment consistently improves task performance while simultaneously enhancing decision reasonability. Our results suggest that aligning models with human-recognized evidence provides a practical path toward more causally plausible decisions, leading to improved robustness and interpretability.

Impact Statement

This work relates to *explanation-guided learning*, a training paradigm that leverages explanation signals as an additional form of supervision beyond labels. A potential positive impact lies in high-stakes and data-scarce domains such as healthcare, where interpretability requirements are stringent and purely label-driven training may amplify spurious correlations. In such settings, explanation-guided learning can provide a practical mechanism to incorporate expert knowledge during training, improve transparency for auditing and debugging, and potentially enhance robustness by discouraging reliance on unintended cues.

However, prior signals can be imperfect and may reflect incomplete or biased human assumptions. If used indiscriminately, explanation-guided learning could constrain models in ways that reduce generalization, suppress valid evidence, or introduce systematic biases. Careful design of explanation supervision, validation across diverse populations, and domain-specific safeguards are therefore essential for responsible use, especially in clinical deployment.

References

Chen, R., Zhang, H., Liang, S., Li, J., and Cao, X. Less is more: Fewer interpretable region via submodular subset selection. In *ICLR*, 2024.

Chen, R., Guo, X., Liu, K., Liang, S., Liu, S., Zhang, Q., Zhang, H., and Cao, X. Where mllms attend and what they rely on: Explaining autoregressive token generation. *arXiv preprint arXiv:2509.22496*, 2025a.

Chen, R., Liang, S., Li, J., Liu, S., Li, M., Huang, Z., Zhang, H., and Cao, X. Interpreting object-level foundation models via visual precision search. In *CVPR*, 2025b.

Chen, R., Liang, S., Li, J., Liu, S., Liu, L., Zhang, H., and Cao, X. Less is more: Efficient black-box attribution via minimal interpretable subset selection. *arXiv preprint arXiv:2504.00470*, 2025c.

Chen, R., Zhang, H., Li, J., Liu, L., Huang, Z., and Cao, X. Generalized semantic contrastive learning via embedding side information for few-shot object detection. *IEEE Transactions on Pattern Analysis and Machine Intelligence*, 47(8):6496–6514, 2025d.

Chen, Y., Chen, R., Zeng, B., Wang, W., Liu, S., Zhang, Q., Hu, Z., Wang, L., Wang, Y., and Cao, X. Did models sufficient learn? attribution-guided training via subset-selected counterfactual augmentation. *arXiv preprint arXiv:2511.12100*, 2025e.

D’Amour, A., Heller, K., Moldovan, D., Adlam, B., Alipanahi, B., Beutel, A., Chen, C., Deaton, J., Eisenstein, J., Hoffman, M. D., et al. Underspecification presents challenges for credibility in modern machine learning. *Journal of Machine Learning Research*, 23(226):1–61, 2022.

Dosovitskiy, A., Beyer, L., Kolesnikov, A., Weissenborn, D., Zhai, X., Unterthiner, T., Dehghani, M., Minderer, M., Heigold, G., Gelly, S., Uszkoreit, J., and Houlsby, N. An image is worth 16x16 words: Transformers for image recognition at scale. In *ICLR*, 2021.

Erion, G., Janizek, J. D., Sturmels, P., Lundberg, S. M., and Lee, S.-I. Improving performance of deep learning models with axiomatic attribution priors and expected gradients. *Nature Machine Intelligence*, 3(7):620–631, 2021.

Feather, J., Durango, A., Gonzalez, R., and McDermott, J. Metamers of neural networks reveal divergence from human perceptual systems. In *NeurIPS*, pp. 10078–10089, 2019.

Gao, S., Li, Z.-Y., Yang, M.-H., Cheng, M.-M., Han, J., and Torr, P. Large-scale unsupervised semantic segmentation. *IEEE Transactions on Pattern Analysis and Machine Intelligence*, 45(6):7457–7476, 2022.

Gao, Y., Gu, S., Jiang, J., Hong, S. R., Yu, D., and Zhao, L. Going beyond xai: A systematic survey for explanation-guided learning. *ACM Computing Surveys*, 56(7):1–39, 2024.

Geirhos, R., Rubisch, P., Michaelis, C., Bethge, M., Wichmann, F. A., and Brendel, W. Imagenet-trained cnns are biased towards texture; increasing shape bias improves accuracy and robustness. In *ICLR*, 2018.

Geirhos, R., Jacobsen, J.-H., Michaelis, C., Zemel, R., Brendel, W., Bethge, M., and Wichmann, F. A. Shortcut learning in deep neural networks. *Nature Machine Intelligence*, 2(11):665–673, 2020.

Han, T., Tu, W.-W., and Li, Y.-F. Explanation consistency training: Facilitating consistency-based semi-supervised learning with interpretability. In *AAAI*, volume 35, pp. 7639–7646, 2021.

He, K., Zhang, X., Ren, S., and Sun, J. Deep residual learning for image recognition. In *CVPR*, pp. 770–778, 2016.

Kauffmann, J., Dippel, J., Ruff, L., Samek, W., Müller, K.-R., and Montavon, G. Explainable ai reveals clever hans effects in unsupervised learning models. *Nature Machine Intelligence*, pp. 1–11, 2025.

Kuznetsov, A., Gyevnar, B., Wang, C., Peters, S., and Albrecht, S. V. Explainable ai for safe and trustworthy autonomous driving: A systematic review. *IEEE Transactions on Intelligent Transportation Systems*, 25(12):19342–19364, 2024.

Li, Y., Chen, Y., Dao, A., Li, L., Cai, Z., Tan, Z., Chen, T., and Kong, Y. Industryqa: Pushing the frontiers of embodied question answering in industrial scenarios. In *NeurIPS*, 2025a.

Li, Y., Lai, Z., Bao, W., Tan, Z., Dao, A., Sui, K., Shen, J., Liu, D., Liu, H., and Kong, Y. Visual large language models for generalized and specialized applications. *arXiv preprint arXiv:2501.02765*, 2025b.

Li, Y., Wang, H., Ding, X., Wang, H., and Li, X. Token activation map to visually explain multimodal llms. In *ICCV*, pp. 48–58, 2025c.

Lundberg, S. M. and Lee, S.-I. A unified approach to interpreting model predictions. In *NeurIPS*, pp. 4765–4774, 2017.

Ngo, R., Chan, L., and Mindermann, S. The alignment problem from a deep learning perspective. In *ICLR*, 2024.

Novello, P., Fel, T., and Vigouroux, D. Making sense of dependence: Efficient black-box explanations using dependence measure. In *NeurIPS*, pp. 4344–4357, 2022.

Petsiuk, V., Das, A., and Saenko, K. Rise: Randomized input sampling for explanation of black-box models. In *BMVC*, pp. 151, 2018.

Pillai, V., Koohpayegani, S. A., Ouligian, A., Fong, D., and Pirsiavash, H. Consistent explanations by contrastive learning. In *CVPR*, pp. 10213–10222, 2022.

Poursabzi-Sangdeh, F., Goldstein, D. G., Hofman, J. M., Wortman Vaughan, J. W., and Wallach, H. Manipulating and measuring model interpretability. In *Proceedings of the 2021 CHI conference on human factors in computing systems*, pp. 1–52, 2021.

Radford, A., Kim, J. W., Hallacy, C., Ramesh, A., Goh, G., Agarwal, S., Sastry, G., Askell, A., Mishkin, P., Clark, J., et al. Learning transferable visual models from natural language supervision. In *ICML*, pp. 8748–8763, 2021.

Ribeiro, M. T., Singh, S., and Guestrin, C. "why should i trust you?" explaining the predictions of any classifier. In *SIGKDD*, pp. 1135–1144, 2016.

Rosenfeld, E., Ravikumar, P. K., and Risteski, A. The risks of invariant risk minimization. In *ICLR*, 2021.

Ross, A. S., Hughes, M. C., and Doshi-Velez, F. Right for the right reasons: training differentiable models by constraining their explanations. In *IJCAI*, pp. 2662–2670, 2017.

Schramowski, P., Stammer, W., Teso, S., Brugger, A., Herbert, F., Shao, X., Luigs, H.-G., Mahlein, A.-K., and Kersting, K. Making deep neural networks right for the right scientific reasons by interacting with their explanations. *Nature Machine Intelligence*, 2(8):476–486, 2020.

Selvaraju, R. R., Lee, S., Shen, Y., Jin, H., Ghosh, S., Heck, L., Batra, D., and Parikh, D. Taking a hint: Leveraging explanations to make vision and language models more grounded. In *ICCV*, pp. 2591–2600, 2019.

Selvaraju, R. R., Cogswell, M., Abhishek, D., Ramakrishna, V., Devi, P., and Dhruv, B. Grad-cam: Visual explanations from deep networks via gradient-based localization. *International Journal of Computer Vision*, 128(2):336–359, 2020.

Simonyan, K., Vedaldi, A., and Zisserman, A. Deep inside convolutional networks: Visualising image classification models and saliency maps. In *ICLR 2014 Workshop*, 2014.

Sun, A., Ma, P., Yuan, Y., and Wang, S. Explain any concept: Segment anything meets concept-based explanation. In *NeurIPS*, pp. 21826–21840, 2023.

Turpin, M., Michael, J., Perez, E., and Bowman, S. Language models don't always say what they think: Unfaithful explanations in chain-of-thought prompting. In *NeurIPS*, pp. 74952–74965, 2023.

Xing, X., Kuo, C.-W., Fuxin, L., Niu, Y., Chen, F., Li, M., Wu, Y., Wen, L., and Zhu, S. Where do large vision-language models look at when answering questions? *arXiv preprint arXiv:2503.13891*, 2025.

Zhang, J., Bargal, S. A., Lin, Z., Brandt, J., Shen, X., and Sclaroff, S. Top-down neural attention by excitation backprop. *International Journal of Computer Vision*, 126(10):1084–1102, 2018.

Zhang, X., Quan, Y., Shen, C., Yuan, X., Yan, S., Xie, L., Wang, W., Gu, C., Tang, H., and Ye, J. From redundancy to relevance: Information flow in lvlms across reasoning tasks. In *NAACL*, pp. 2289–2299, 2025a.

Zhang, Y., Gu, S., Gao, Y., Pan, B., Yang, X., and Zhao, L. Magi: Multi-annotated explanation-guided learning. In *Proceedings of the IEEE/CVF International Conference on Computer Vision*, pp. 1977–1987, 2023.

Zhang, Y., Jiang, T., Pan, B., Wang, J., Bai, G., and Zhao, L. Megl: Multimodal explanation-guided learning. *arXiv preprint arXiv:2411.13053*, 2024.

Zhang, Y., Song, J., Gu, S., Jiang, T., Pan, B., Bai, G., and Zhao, L. Saliency-bench: A comprehensive benchmark for evaluating visual explanations. In *SIGKDD*, pp. 5924–5935, 2025b.

Zhang, Z., Lu, Y., Fu, Y., Huo, Y., Yang, S., Wu, Y., Si, H., Cong, X., Chen, H., Lin, Y., et al. Agentcpm-gui: Building mobile-use agents with reinforcement fine-tuning. *arXiv preprint arXiv:2506.01391*, 2025c.

Zhao, C., Wang, K., Zeng, X., Zhao, R., and Chan, A. B. Gradient-based visual explanation for transformer-based clip. In *ICML*, pp. 61072–61091, 2024.

A. More Details for GUI-Agent Experiments

A.1. Dataset Format

Each sample is stored as a JSON object containing an `id`, a screenshot reference (`image`), and a multi-turn conversations list in a `system/user/assistant` format. The assistant output follows a strict action schema and includes a `thought` field (`thinking`) and an executable action such as a click `POINT` (`decision`). In addition, each sample provides a human-annotated `bounding_box` for the target UI element, which serves as a human prior for alignment and evaluation. All GUI tasks are collected and executed in Chinese, and the paper presents an English-translated version of the prompts for clarity.

```
{
  "id": "0",
  "image": {
    "<image_00>": "img/screenshot_0.jpg"
  },
  "conversations": [
    {
      "role": "system",
      "content": "# Role\nYou are an agent familiar with Android touch-based GUI operations. Given a user's request, analyze the GUI elements and layout on the current screen and produce the next action.\n\n# Task\nGiven the current screenshot, output the next operation to accomplish the user request.\n\n# Rule\n- Output in compact JSON format.\n- The action must follow the Schema constraints.\n\n# Schema\n{\n  \"type\": \"object\",\n  \"description\": \"Execute an action and decide the task status\",\n  \"additionalProperties\": false,\n  \"optional\": [\n    \"thought\"\n  ],\n  \"properties\": {\n    \"thought\": {\n      \"type\": \"string\",\n      \"description\": \"The agent's reasoning\"\n    },\n    \"POINT\": {\n      \"$ref\": \"#/defs/Location\"\n    },\n    \"to\": {\n      \"description\": \"Movement / gesture parameters\"\n    },\n    \"oneOf\": [\n      {\n        \"enum\": [\n          \"up\",\n          \"down\",\n          \"left\",\n          \"right\"\n        ],\n        \"description\": \"Swipe from the current point (POINT) in one of four directions\"\n      },\n      {\n        \"$ref\": \"#/defs/Location\"\n      },\n      {\n        \"description\": \"Move to a specific location\""
    },\n    \"duration\": {\n      \"type\": \"integer\"\n    },\n    \"description\": \"Execution or wait time in milliseconds\"\n  },\n  \"minimum\": 0,\n  \"default\": 200,\n  \"PRESS\": {\n    \"type\": \"string\",\n    \"description\": \"Press a special key\"\n  },\n  \"enum\": [\n    \"HOME\",\n    \"BACK\",\n    \"ENTER\"\n  ],\n  \"TYPE\": {\n    \"type\": \"string\",\n    \"description\": \"Input text\"\n  },\n  \"STATUS\": {\n    \"type\": \"string\",\n    \"description\": \"Task status: satisfied (no action needed), impossible, interrupt, need_feedback\"\n  },\n  \"enum\": [\n    \"continue\",\n    \"finish\",\n    \"satisfied\",\n    \"impossible\",\n    \"interrupt\"\n  ],\n  \"description\": \"These values are relative to the top-left corner and scaled to [0,1000]; the first entry is x and the second is y\"\n},\n  \"items\": {\n    \"type\": \"integer\",\n    \"minimum\": 0,\n    \"maximum\": 1000\n  },\n  \"minItems\": 2,\n  \"maxItems\": 2
  },
  {
    "role": "user",
    "content": "<Question>Search bilibili.com, then search for 'Qianting Weiwei Mi' on the website and open the uploader list. Add the page to bookmarks and verify it appears in the bookmark manager.</Question>\n\n# Current screenshot: <image_00>\n\n"
  },
  {
    "role": "assistant",
    "content": "{\n  \"thought\": \"Locate and tap the browser icon on the home screen to open the browser.\",\n  \"POINT\": [591, 915]\n}"
  }
  ],
  "bounding_box": [706, 2438, 858, 2590]
}
```

A.2. Attributing Thinking and Decision

Unlike approaches that attribute only the final action, this work treats a mobile agent's *reasoning process* (`thinking`) and *executed action* (`decision`) as a unified decision chain for attribution analysis. Concretely, given model parameters θ and

input X , the proposed high-faithfulness attribution method EAGLE is used to jointly attribute the visual evidence relied upon when generating \hat{Z} (the reasoning sequence) and \hat{A} (the final action decision):

$$\mathcal{A} = \mathcal{A}(f_\theta, X, \{\hat{Z}, \hat{A}\}), \quad (6)$$

where $\mathcal{A}(\cdot)$ denotes the attribution operator and outputs a single attribution heatmap that quantifies the contribution of different screen regions to the *overall reasoning–decision process*. This attribution does not separate intermediate stages of reasoning and decision-making; instead, it directly captures the key set of visual evidence the model relies on to complete the current task. Owing to the explicit and stable spatial layout in GUI environments, the resulting attribution can be naturally mapped to screen coordinates, providing a unified and actionable supervision signal for subsequent attribution alignment and reliability-enhancing training.

A.3. Training Procedure

To control computational overhead, the attribution alignment loss is computed periodically rather than at every update step. Specifically, at pre-defined steps, the current model attributions are computed, the Top- k salient regions are extracted, and their overlap with the target action region is examined. If the salient attributed regions fail to sufficiently cover the target region, an attribution alignment penalty is applied. Algorithm 2 provides a formal description.

Algorithm 2 Attribution-guided training for reliability enhancement of GUI agents

Input: training sample (X, I, Z, A, B) where I is the screenshot, Z is thinking, A is the action decision, and B is the target UI bounding box; attribution operator $\mathcal{A}(\cdot)$; attribution interval K ; top- k regions k (set to $k = 2$).

Output: trained model parameters θ .

Initialize model parameters θ

for $t = 1$ **to** T_{\max} **do**

- Predict thinking \hat{Z} and action \hat{A} under current θ
- Compute supervised loss \mathcal{L}_{CE} {SFT cross-entropy loss}
- if** $t \bmod K = 0$ **then**

 - Compute joint attribution map $\mathcal{A} \leftarrow \mathcal{A}(f_\theta, I, \{\hat{Z}, \hat{A}\})$
 - Extract Top- k salient regions $\mathcal{S} = \{S_1, \dots, S_k\}$ from \mathcal{A}
 - Initialize $\mathcal{L}_{\text{attr}} \leftarrow 0$
 - for** $i = 1$ **to** $|\mathcal{S}|$ **do**

 - if** $S_i \not\subset B$ **then**
 - $\mathcal{L}_{\text{attr}} \leftarrow \mathcal{L}_{\text{attr}} + \text{Penalty}$
 - break**
 - end if**
 - if** $\text{Area}(S_i \cap B) / \text{Area}(B) \geq 0.75$ **then**
 - break**
 - end if**

 - end for**
 - $\mathcal{L}_{\text{total}} \leftarrow \mathcal{L}_{\text{CE}} + \mathcal{L}_{\text{attr}}$
 - else**
 - $\mathcal{L}_{\text{total}} \leftarrow \mathcal{L}_{\text{CE}}$
 - end if**
 - Update θ using $\nabla_\theta \mathcal{L}_{\text{total}}$

end for

A.4. Evaluation Metrics

Two metrics are used to evaluate the GUI agent clicking task: click success rate and distance error. The **click success rate** measures whether the predicted click point falls inside the human-annotated target bounding box. The **distance error** quantifies how far the predicted point is from the ground-truth target region: it is set to 0 if the predicted point lies inside the bounding box; otherwise, it is computed as the minimum Euclidean distance from the point to the bounding box boundary (i.e., the closest point on the box). Figure 7 illustrates these metrics with representative examples.

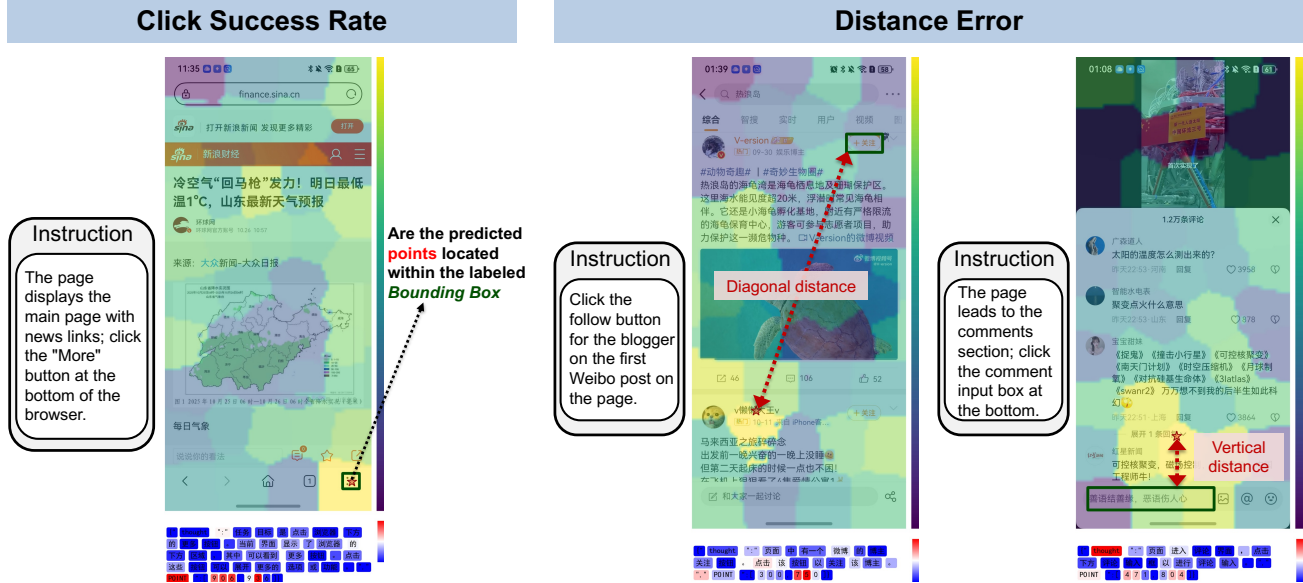


Figure 7. Illustration of evaluation metrics for the GUI agent clicking task. *Click Success Rate* counts a prediction as successful if the predicted click point falls inside the labeled target UI element bounding box. *Distance Error* measures the distance between the predicted click point and the target location (e.g., to the bounding box or target point), with examples showing diagonal and vertical distances.

B. Limitations and Future Work

Limitations. Our method depends heavily on the quality and coverage of human-prior annotations. In large-scale settings, such fine-grained human labels are often unavailable or prohibitively expensive, and coarse or noisy priors may weaken the training signal and limit scalability.

Future work could mitigate this by developing scalable, automated prior acquisition schemes (e.g., weak/self-supervised cues, pseudo-labels from detection/segmentation models, or priors distilled from multi-model consensus). Another promising direction is to integrate attribution into reinforcement learning, using attribution-based signals to select or refine more evidence-consistent chains of thought (e.g., incorporating “evidence rationality” into the reward), thereby encouraging more reliable reasoning and decision-making.